ACS Catalysis

Research Article

pubs.acs.org/acscatalysis

Trends in Selective Hydrogen Peroxide Production on Transition Metal Surfaces from First Principles

Rees B. Rankin and Jeffrey Greeley*

Center for Nanoscale Materials, Argonne National Laboratory, 9700 South Cass Avenue, Argonne, Illinois 60439, United States

Supporting Information

ABSTRACT: We present a comprehensive, density functional theory based analysis of the direct synthesis of hydrogen peroxide, H_2O_2, on 12 transition metal surfaces. We determine the full thermodynamics and selected kinetics of the reaction network on these metals, and we analyze these energetics with simple, microkinetically motivated rate theories to assess the activity and selectivity of hydrogen peroxide production on the surfaces of interest. By further exploiting Brønsted–Evans–Polanyi relationships and scaling relationships between the binding energies of different adsorbates, we express the results in the form of a two-dimensional contour volcano plot, with the activity and selectivity being determined as functions of two independent descriptors: the atomic hydrogen and oxygen adsorption free energies. We identify both a region of maximum predicted catalytic activity, which is near Pt and Pd in descriptor space, and a region of selective hydrogen peroxide production, which includes Au. The optimal catalysts represent a compromise between activity and selectivity and are predicted to fall approximately between Au and Pd in descriptor space, providing a compact explanation for the experimentally known performance of Au–Pd alloys for hydrogen peroxide synthesis, and suggesting a target for future computational screening efforts to identify improved direct hydrogen peroxide synthesis catalysts. Related methods of combining activity and selectivity analysis into a single volcano plot may be applicable to, and useful for, other aqueous phase heterogeneous catalytic reactions where selectivity is a key catalytic criterion.

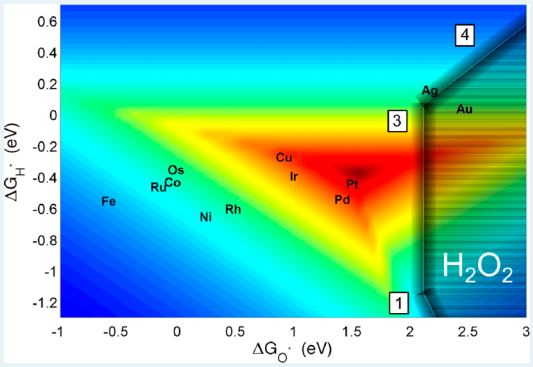

KEYWORDS: *density functional theory, oxygen reduction reaction, selectivity, hydrogen peroxide, volcano*

1. INTRODUCTION

The direct synthesis of hydrogen peroxide, H_2O_2, from hydrogen and oxygen is both an industrially relevant process for producing this important commodity chemical and a classic example of the need to balance activity and selectivity considerations to achieve desired heterogeneous catalytic syntheses. Well-established approaches to peroxide production have employed the anthraquinone synthesis mechanism,[1] which produces significantly more concentrated H_2O_2 solutions than are generally required for most applications. Higher-efficiency direct synthesis processes, on the other hand, have recently shown substantial promise in overcoming these drawbacks; Pd–Au,[2−6] acid-promoted Pd–Au nanoparticles,[4] acidic halide-promoted systems,[7−9] and even zeolite-supported catalysts[10,11] have all been investigated, and the best Pd–Au catalysts show hydrogen peroxide selectivities approaching 100%.[4] These experimental investigations have been complemented by a limited number of computational analyses, including studies of the thermodynamics of Au–Pd surface alloys for the adsorption of hydrogen peroxide-related intermediates.[12−14] In spite of this progress, however, important challenges remain in the understanding and design of catalysts for direct hydrogen peroxide synthesis. From a fundamental scientific perspective, a comprehensive framework in which both catalytic activity and selectivity to peroxide at liquid–solid interfaces can be evaluated for a broad range of metals and alloys is needed, and from a practical industrial perspective, the development of lower-cost alternatives to current precious metal catalysts is of interest.

The development of descriptor-based computational analysis, and in particular volcano plot analysis, has recently emerged as a powerful tool for both the elucidation of fundamental reactivity trends across transition metal alloys and the identification of enhanced catalytic materials via computational catalyst screening. This approach has been successful, for example, in finding improved platinum-based alloys for the electrochemical reduction of oxygen[15−23] (a process that is not dissimilar, in some ways, to the heterogeneous production of hydrogen peroxide) and in providing important insights into the ammonia decomposition,[24] hydrodesulfurization,[25] and hydrogen evolution[21,26,27] reactions, as well as methanol decomposition[28] and even biomass-related reactions,[29] among others. Few such analyses, however, have attempted to incorporate selectivity considerations into the volcano-based descriptions,[30,31] and the development of easy-to-interpret computational screening strategies that explicitly account for selectivity considerations remains an important challenge.

Received: May 29, 2012
Revised: October 9, 2012
Published: October 19, 2012

   dx.doi.org/10.1021/cs3003337 | ACS Catal. 2012, 2, 2664–2672

In the present study, we present a detailed examination of how density functional theory (DFT) calculations can be employed to generate volcano plots that explicitly incorporate both activity and selectivity criteria at liquid−solid interfaces in a descriptor-based approach. Through a careful analysis of calculated reaction free energies for a variety of transition metals, we generate predictions of the activity of metals and alloys for direct reduction of oxygen with H_2 as a function of two independent descriptors: the atomic hydrogen and oxygen binding energies. Using simple free energy inequalities related to branch points in the reaction network, we further identify regions of this volcano plot where selective production of hydrogen peroxide is likely to be favored. We briefly describe the effect of steps and defects on these activity and selectivity properties, and we indicate how the results both explain the performance of catalytic alloys for direct hydrogen peroxide synthesis that have been experimentally identified to date and suggest important strategies for further catalyst optimization via computational screening.

2. COMPUTATIONAL METHODS AND CALCULATION DETAILS

This work employed plane-wave density functional theory calculations as implemented in the Vienna Ab Initio Simulation Package (VASP).[32−35] The calculations used the PAW[36,37] treatment of core electrons, together with the PW91-GGA[38,39] density functional. A minimum k-point grid sampling of 4 × 4 × 1 was used; in all cases, convergence with respect to the k-point grid was verified. The PREC=HIGH accuracy extension in VASP was employed with a cutoff energy of ∼520 eV, FFT mesh grids large enough to avoid wraparound errors, and a default Methfessel−Paxton[40] Fermi smearing of 0.2 eV. We have selected a broad periodic block of transition metal (TM) elements, including Fe, Co, Ni, Cu, Ru, Rh, Pd, Ag, Os, Ir, Pt, and Au, for analysis. All calculations were performed fully spin-polarized, since it is known that magnetic considerations can be significant for certain oxygen-based adsorbates and transition states, even on inherently nonmagnetic surfaces.[41−43] The fcc(111), bcc(110), and hcp(0001) surfaces were employed for the close-packed surfaces (we note that the Fe bcc(110) surface is only quasi-hexagonally close packed in relation to the fcc(111) and hcp(0001) surfaces of the other TM elements considered; however, its structure is sufficiently similar for inclusion in our trends analysis), while selected fcc(211) surfaces were considered for step calculations. Generally good agreement between calculated and experimental lattice constants of these TM species is seen in the Supporting Information, Table SI.1 (for the magnetic metals, we also report the net magnetic moments per atom); a slight overestimation of the lattice constant for the highly noble metals, as well as for Pd and Pt, is a known issue with this approach but does not affect calculated reactivity trends.

A four-layer, 2 × 2 surface supercell was employed (the top two layers on the adsorbate side were allowed to relax) for the close-packed surfaces. To examine the sensitivity of this model slab with respect to convergence and coverage effects for oxygen and hydroxyl adsorption on selected metals, we have performed additional tests with different k-point grids, slab thicknesses, and surface coverages (see the Supporting Information for details). When we increase the k-point resolution to a 6 × 6 × 1 grid and the slab thickness to six layers, the changes in the binding energies for these species are found to be small (less than 0.1 eV in all cases). When increasing the surface coverage to 1/3 monolayer (ML) (fcc(111)-$(\sqrt{3} \times \sqrt{3})R30°$ unit cell) on Pt(111) and Au(111), we observed binding energy shifts of about 0.3 eV for oxygen (weaker binding) and between −0.1 and −0.25 eV for hydroxyl (stronger binding). At higher coverages, which might be found, for example, on metals susceptible to poisoning, these results imply a modestly increased thermodynamic driving force toward hydrogenation of oxygen, combined with a decreased driving force for water formation. A 3 × 2 surface cell, with four layers perpendicular to the terrace planes, was used for the (211) stepped surfaces. The vacuum spacing was set to approximately 20 Å to ensure no z-axis interactions between neighboring cell images. Geometric optimization of the near-surface atoms and adsorbates was performed with a force-convergence criterion of <0.035 eV/Å per atom, while self-consistent iteration on the electronic wave function was performed with a convergence criterion of 1.5×10^{-7}. For the adsorbates studied, initial placement prior to geometric optimization was performed via location above the four high-symmetry sites (fcc, hcp, top, and bridge), with adsorbate rotational symmetry considered via 30−45−60° rotation operations (relative to the surface normal), as necessary. To characterize activation barriers along the reaction paths, nudged elastic band (NEB) calculations were performed with the climbing-image implementation in the VTST extension of the VASP code developed by Henkelman et al;[44−47] all transition states have been verified by frequency analyses. Due to the known problem of DFT in accounting for the O_2 gas phase energy, a correction (0.41 eV) was made to reproduce the experimental free energy of formation of liquid H_2O.[48] Additionally, an average binding energy correction of −0.45 eV per adsorbate was applied to selected surface bound species (OH, OOH, H_2O_2) to reflect the effect of hydrogen bonding to surrounding water bilayers. This value was taken from calculations performed of the excess hydrogen bonding energy of OH* in the water bilayer on Pd, Pt, Ag, and Au(111). The value is similar to that found in prior work.[48] Entropies are taken from thermodynamic tables at 298 K. We assume that the degree of hydrogen bonding is approximately constant between the transition states and the reactant/product states, implying that net changes in the water corrections are small for reaction activation barriers. The free energy of H_2O_2(aq) is taken as the value from the standard electroreduction equilibrium potential.[49] Volcano contour surface plots shown are made with Matlab software with default three-dimensional plot settings and 0.01 eV sampling resolution per descriptor.

3. RESULTS AND DISCUSSION

3.1. Reaction Network Free Energy Analysis and the Direct H_2O_2 Synthesis Pathway. The reaction network considered for heterogeneous oxygen reduction and hydrogen peroxide synthesis is shown schematically in Figure 1. A pathway leading to direct formation of H_2O_2 through sequential hydrogenation of molecular oxygen, followed by desorption prior to dissociation, is seen on the left side of the diagram; we refer to this pathway as the direct hydrogen peroxide synthesis pathway (DHPSP). Pathways which result in the formation of water, or possibly even surface oxides, on the other hand, are found toward the right, and reaction steps by which the H_2O_2-selective pathway may be diverted to water formation, including oxygen−oxygen bond cleavage in H_2O_2 or its precursors, are indicated by horizontal arrows. Additionally, for each hydrogenation step, we have considered a parallel pathway (not explicitly shown in Figure 1) whereby hydrogenation can occur via a water-mediated surface step with simultaneous creation of a new surface OH* (for example, instead of considering only O* +

dx.doi.org/10.1021/cs3003337 | ACS Catal. 2012, 2, 2664−2672

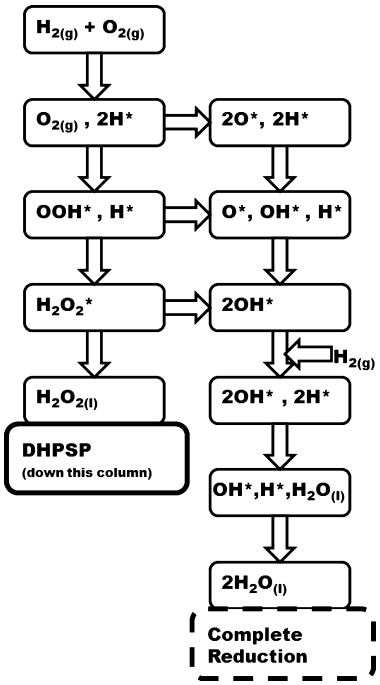

Figure 1. Schematic diagram of selected elementary steps in the reaction network for direct oxygen reduction from $H_2 + O_2$ to H_2O_2 or H_2O in the aqueous phase. In some cases, for clarity, gaseous and liquid phase reactants and products, together with vacant surface sites, are not explicitly shown. An asterisk indicates surface-adsorbed species. For all hydrogenation steps we have also considered water-mediated hydrogenation events ($O_X^* + * + H_2O \rightarrow HO_X^* + OH^*$) which are not explicitly depicted in the figure (see the text for more details).

$H^* \rightarrow OH^* + *$, we also consider $O^* + * + H_2O_{(l)} \rightarrow 2OH^*$, where the "$*$" notation indicates either a vacant surface site or a surface-adsorbed species). However, we find that these water-mediated hydrogenations are only thermodynamically favorable when $G_{H_2O} > G_{H^*} + G_{OH^*}$, where the free energy of H_2O is in the liquid phase; this criterion is only fulfilled in a region of descriptor space (see discussion below) that is not of interest for direct peroxide synthesis, and so we do not consider these events further in this analysis. In Figure 2, we present the predicted rate constants for the following elementary steps:

$$H_{2(g)} + 2* \rightarrow 2H^*$$

$$O_{2(g)} + 2* \rightarrow 2O^*$$

$$OOH^* + * \rightarrow O^* + OH^*$$

$$H_2O_2^* + * \rightarrow 2OH^*$$

$$H^* + O^* \rightarrow OH^* + *$$

$$H^* + O_{2(g)} \rightarrow OOH^*$$

$$H^* + OOH^* \rightarrow H_2O_2^* + *$$

$$H^* + OH^* \rightarrow H_2O_{(l)} + 2*$$

$$H_2O_2^* \rightarrow H_2O_{2(aq)} + *$$

Figure 2 shows the data for all considered transition metals; the results are given as $\log_{10}[\text{rate}/(k_BT/h)]$, where k_B is Boltzmann's constant, h is Planck's constant, and k_BT/h ($\sim 6 \times 10^{12}$ s^{-1} at 298 K) is taken as the elementary prefactor and is used to scale all rates (in the Supporting Information, we show results for a few prefactors computed directly from vibrational frequency analysis; these more detailed calculations reveal a maximum divergence of $^1/_2$ order of magnitude from the assumed prefactors); the elementary rates are assumed to be irreversible unless otherwise stated (see additional discussion below). The metals in Figure 2a are the most oxophilic, with increasing strength of oxygen binding from the top to the bottom; the metals in Figure 2b are the six least oxophilic—with the same oxygen binding trend from top to bottom. In our rate theory and energetic analyses, we use Brønsted–Evans–Polanyi and scaling relationships to estimate energetic quantities, as described further in the Supporting Information. For elementary steps involving dissociative adsorption of a molecule from the gas or liquid phase, it is assumed that the dissociating transition state has no entropy, and for elementary steps involving only surface-bound species, entropy changes are assumed to be zero. We also assume that H_2O_2 desorption has a prefactor of k_BT/h, the same prefactor that is used for the other free energy-based elementary step rates, and is irreversible. Desorption of water product, on the other hand, is assumed to be in quasi-equilibrium. These assumptions are motivated by the fact that, in a liquid environment, the bulk concentration of water will be high, thus promoting water readsorption. Unless significant hydrogen peroxide accumulates in solution, however, a driving force for readsorption will not be present. This effective irreversibility for peroxide desorption will be valid for practical catalysts where there has not been significant peroxide accumulation in solution. We note that, for the other elementary steps in the reaction network, the assumption of irreversibility may lead to modest quantitative (although likely not qualitative) inaccuracies in our kinetic model; such effects are likely to be most significant far from the volcano maximum, where surface coverages may deviate substantially from order unity (poisoning, for example, may occur in the strong-binding regions of the volcano). Finally, for the elementary hydrogenation steps, we have assumed that the overall reaction barriers are equivalent to the thermodynamic barriers (with appropriate entropy corrections), when those barriers are positive, and are essentially zero when the elementary reaction free energies are exothermic. This approach implicitly assumes that water and hydrogen bonding in an aqueous environment facilitate hydrogen transfer and significantly decrease kinetic overbarriers for hydrogenation; similar water- or OH-assisted hydrogen transfer phenomena have been described in the literature.[15,50−52] Additional details on our energy and rate analyses can be found in the Supporting Information, and raw adsorption free energy values are given in Table 1.

The results, which provide a generalization of existing treatments on more limited sets of metals,[12] demonstrate several key features which point toward trends in predicted activity and selectivity of catalysts for the aqueous phase heterogeneous reduction of O_2 by H_2. For example, highly oxophilic metals such as Fe and Ru are likely to experience surface poisoning by O* and OH* because the OH* removal step (to produce H_2O) has a very low predicted rate, with $\log_{10}[\text{rate}/(k_BT/h)] < -20$. Similarly, metals such as Cu, and in particular Pd and Pt, are seen to show a balance of several rate constants of intermediate magnitude for most of the possible elementary steps considered. This implies that, regardless of pathway, overall activity will likely be high, while selectivity may be complex to interpret. Highly noble metals such as Au show difficulty in breaking O_2, O–OH, and HO–OH bonds, while the opposite trend is found on metals

dx.doi.org/10.1021/cs3003337 | ACS Catal. 2012, 2, 2664−2672

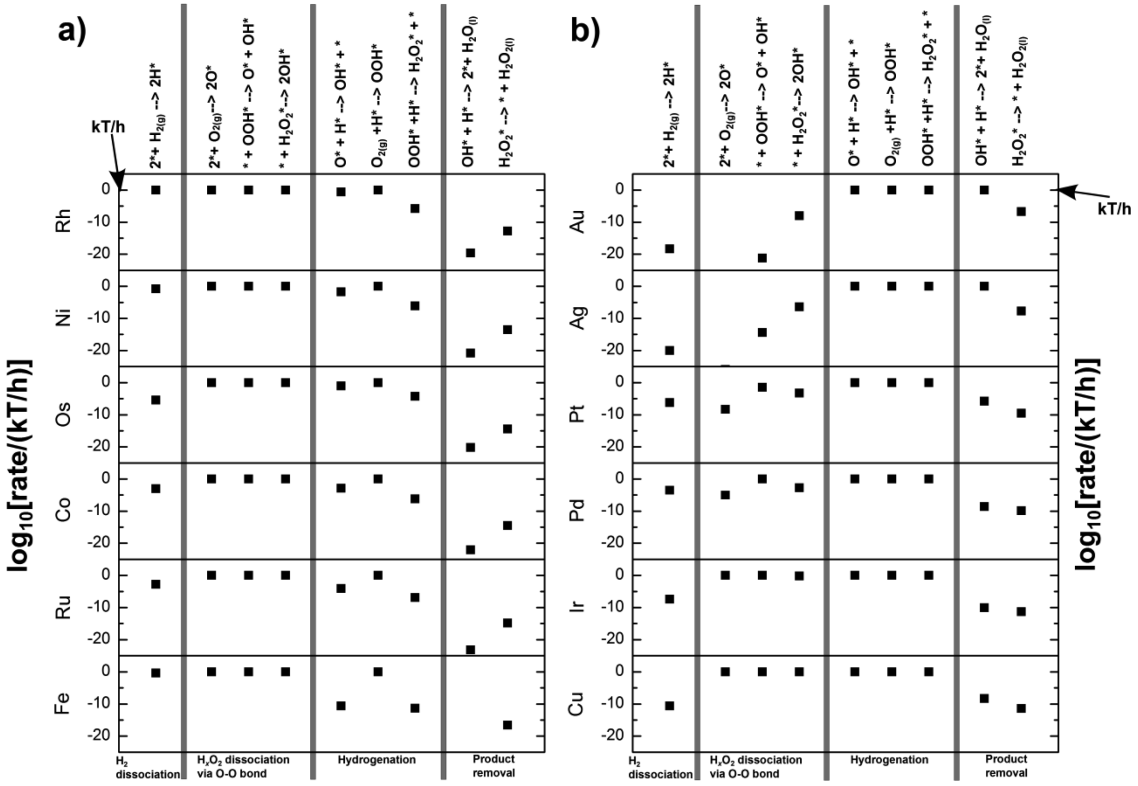

Figure 2. Predicted rate constants for various reaction steps on the closest-packed surfaces of 12 transition metals. In (a), the six most oxophilic metals are given (stronger oxygen binding from the top to the bottom). Similarly, in (b), the six least oxophilic metals are given. For each metal and reaction mechanistic step, the predicted rate constant is scaled relative to k_BT/h, and given in log(10) units; thus rates of "0" in this plot correspond to reaction mechanism steps with essentially no barrier. Rates that are less than −25 in this scale not shown. Data are determined from derived scaling relations and BEP equations.

Table 1. DFT-Computed Free Energies of the Various Surface Species on the Transition Metal Surfaces Examined[a]

	adsorbate species free energy				
transition metal surface	H*	O*	OH*	OOH*	H_2O_2*
Fe(110)	−0.72	−0.80	−1.32	2.66	N/A
Ru(0001)	−0.62	−0.24	−0.62	2.97	N/A
Co(0001)	−0.61	−0.13	−0.81	N/A	N/A
Os(0001)	−0.52	−0.10	−0.43	3.23	N/A
Ni(111)	−0.70	0.18	−0.62	3.43	2.95
Rh(111)	−0.75	0.41	−0.46	3.10	2.85
Cu(111)	−0.31	0.84	−0.49	3.23	3.10
Ir(111)	−0.44	0.88	0.03	3.41	2.93
Pd(111)	−0.59	1.35	0.23	3.85	3.08
Pt(111)	−0.49	1.46	0.37	3.85	3.20
Ag(111)	0.06	2.04	−0.06	3.86	3.31
Au(111)	0.00	2.34	0.72	4.30	3.24

[a]Units of free energy are given are in eV relative to the free energy of stoichiometrically appropriate amounts of $H_2O_{(l)}$ and $H_{2(g)}$. For reference, the energy of $2H_{2(g)} + O_{2(g)}$ relative to $2H_2O_{(l)}$ is 4.92 eV. Where listed as "N/A", a stable low energy state of the adsorbate could not be found in the calculations. An asterisk indicates a surface-adsorbed species. Additional information on entropies and zero point energies is given in the Supporting Information.

like Fe and Ru. In fact, we can see that, around Au and Ag, there is an inversion in the activity of the elementary steps involving H_2O_2*: the predicted rates for dissociation (to 2OH*) become less than the predicted rates for desorption to the solution phase.

While the above observations are initially useful in helping to predict activity and selectivity of single-element transition metal catalysts, a more detailed analysis is required to fully understand the relevant activity and selectivity trends. Below, we present such an analysis by further characterizing the reaction network using a technique known as Sabatier analysis, determining descriptors for activity and selectivity, commenting on the effect of surface structural inhomogeneities on the predicted catalytic properties, and relating our results to state-of-the-art experimental analyses of direct hydrogen peroxide production.

3.2. Descriptor Analysis and Sabatier Volcano. The general concept of the Sabatier analysis provides simple descriptions of the kinetics of certain heterogeneous catalytic reactions, including the electrochemical oxygen reduction reaction (ORR).[41,48,53,54] This approach, in which idealized coverages are assumed for reactive intermediates,[55] gives upper bounds for reaction rates and has successfully described trends in electrochemical ORR activity in terms of a single descriptor, $\Delta E_{b,O}$ (the binding energy of oxygen). Platinum lies at or nearly at the peak of this electrochemical Sabatier volcano (in agreement with known experimental findings),[54] even when the volcano analysis is studied with respect to sensitivity to coverage assumptions,[15] and as we describe further below, there are some analogies between the electrochemical oxygen reduction analysis and our heterogeneous oxygen reduction analysis. However, we note that, because our reaction network is heterogeneous, not electrochemical, it also involves the explicit adsorption of atomic hydrogen, whose binding energy does not correlate well with the corresponding energy of atomic oxygen on the metal surfaces, our analysis, described below, will yield a

dx.doi.org/10.1021/cs3003337 | ACS Catal. 2012, 2, 2664−2672

multidimensional volcano with two descriptors, ΔG_{O*} and ΔG_{H*}.

For each considered reaction mechanism (Figure 1) on each metal, we identify the elementary step with the least favorable free energy, which we interpret as the rate-limiting step for that reaction mechanism on that transition metal. We then determine the mechanism with the most favorable rate-limiting step for each transition metal, and we take the negative of the free energy barrier to be a measure of the effective activity. Having performed this analysis, it is possible to quickly generate a spline fit to the calculated activities and to interpolate a Sabatier volcano based on the chosen descriptors (ΔG_{O*} and ΔG_{H*}). This method gives an approximate tool to derive a Sabatier volcano, but it is subject to the particular choice of spline-fitting method and to statistical factors arising from sparsity in the data set. We therefore choose to focus on a linearized volcano derived from scaling correlations between adsorbate energies and from Brønsted–Evans–Polanyi (BEP) relationships,[22,56] which correlate the transition state (kinetic) and final state (thermodynamic) reaction energies of given elementary steps on different transition metals. As described below, this approach relies only on well-justified approximations from fundamental physical and chemical principles and provides simple yet powerful insights into the key catalytic properties of the considered systems.

For each of the surface-bound adsorbates, a correlation of the binding energy to the appropriate descriptor is determined; generally, the adsorbate binding energy will correlate with the binding energy of the atomic species through which the adsorbate binds to the metal surface[57] (see Supporting Information for full details on the correlations). Additionally, BEP relations for the following elementary dissociation reactions are determined via explicit DFT calculations on the surfaces of Ag, Au, Cu, Pd, Pt, and Ru. These metals are chosen so that the BEP relationship will include metals spanning a reasonable range of the total descriptor space:

$$H_{2(g)} + 2* \rightarrow 2H*$$

$$O_{2(g)} + 2* \rightarrow 2O*$$

$$OOH* + * \rightarrow O* + OH*$$

$$H_2O_2* + * \rightarrow 2OH*$$

Once these elementary energetic analyses are in place, the energies of all mechanistic steps at each value of ΔG_{O*} and ΔG_{H*} can be rapidly evaluated via the thermodynamic correlations or BEP relations, and the corresponding Sabatier activity can be determined. The results of this analysis are shown in Figure 3. We note that, near the very peak of the volcano, we do not allow for negative implied barriers in the rate-limiting step. This produces a small region of essentially zero barrier near the top of the volcano; in a full microkinetic analysis, coverage effects, together with small hydrogenation overbarriers, would modestly decrease the rate near the top of the volcano.[58] Similar to the electrochemical oxygen reduction volcano,[48,53] Pt and Pd are seen to have very high predicted activities, while Au/Ag and Ru/Co lie on opposite sides of the volcano and have significantly lower activities.

In Figure 4, we show the predicted rate-controlling step for each region of descriptor space. Four such regions are identified. Where hydrogen binds very weakly, H_2 dissociation is the rate-limiting step for a range of oxygen adsorption free energies; Au and Ag fall into this region. Where both oxygen and hydrogen

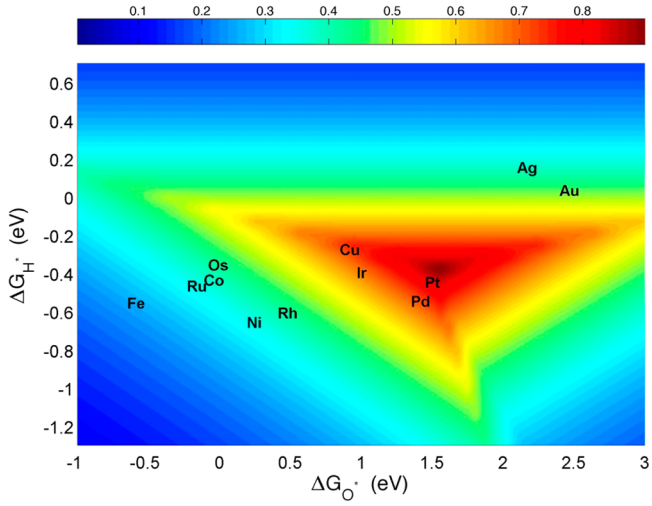

Figure 3. Linearized activity volcano for direct oxygen reduction. ΔG_{O*} and ΔG_{H*} are the free energies of oxygen and hydrogen adsorption, respectively, referenced to liquid water and gaseous H_2. Dark red indicates maximum predicted activity. The activity, in eV, is normalized by k_BT/h in a style similar to Nørskov et al.[48]

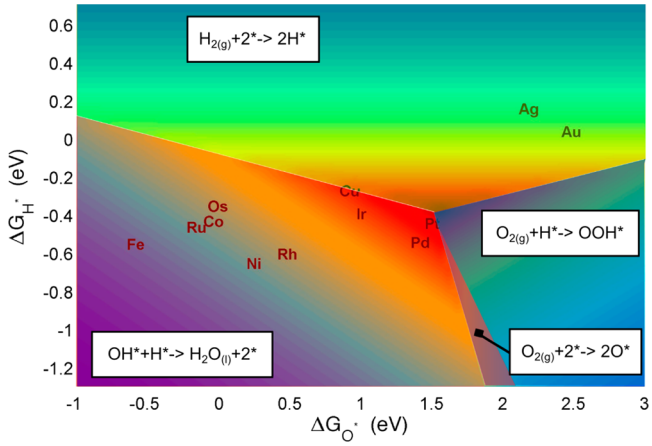

Figure 4. Rate-controlling steps in heterogeneous catalytic oxygen reduction. ΔG_{O*} and ΔG_{H*} are the free energies of oxygen and hydrogen adsorption, respectively, referenced to liquid water and gaseous H_2. In the above regions, the predicted rate-limiting steps (RLS) in each region of descriptor space are shown. The width (or existence) of the O_2 dissociation region is highly sensitive to the BEP equation employed. The color scale of the underlying volcano is the same as in Figure 3, while each region is given an arbitrary overlay of half-transparent color to increase visual contrast.

bind strongly, on the other hand, hydrogenation of OH* to water is the predicted rate-limiting step; Ru, Rh, and Ni, for example, lie in this region (we note that, due to coverage effects that are not explicitly accounted for in our Sabatier analysis, these metals may in reality be oxide covered under realistic reaction conditions). Cu and Ir are predicted to lie near the intersection of the regions in Figure 4 where H_2 dissociation and OH* hydrogenation are predicted to be rate limiting. In regions of the volcano where hydrogen binds strongly but oxygen binds weakly, two different rate-limiting regions are found. Both rate-limiting steps involve the formation of product species from $O_{2(g)}$ but proceed through different mechanistic processes. In the more strongly oxygen binding (leftmost) portion of this region of the volcano, a small area is predicted where dissociation of $O_{2(g)}$ to 2O* is limiting,

dx.doi.org/10.1021/cs3003337 | ACS Catal. 2012, 2, 2664–2672

while OOH* formation from H* + $O_{2(g)}$ becomes the relevant rate-limiting step as the oxygen binding free energy becomes weaker.

3.3. Descriptor Analysis and Sabatier Volcano: Selectivity Considerations. The Sabatier-based activity analysis presented above provides guidance as to what catalysts are likely to be active for heterogeneous oxygen reduction in nonelectrochemical aqueous environments, but additional considerations are required to determine what metals and alloys will selectively form hydrogen peroxide compared to water. Several of the rate-limiting regions in Figure 4 (H_2 dissociation and OOH formation) are consistent with the possibility of H_2O_2 formation, but our activity analysis alone is not sufficient to determine selectivity between reaction pathways that diverge after the rate-determining steps. From Figure 1, for example, it can be seen that, even if OOH formation is favored, subsequent dissociation to O* + OH* (ultimately leading to water formation), or further hydrogenation to H_2O_2*, followed by dissociation, may occur.

To incorporate selectivity considerations into our analysis, we identify a set of free energy inequalities associated with certain of the reactive intermediates in Figure 1. These inequalities correspond to reactions involving O−O bond cleavage that will divert the catalyst in question away from the DHPSP. In order for the system to be fully selective toward H_2O_2, all of the selectivity free energy inequalities (constraints) must be satisfied—that is, the selective hydrogen peroxide region of the Sabatier volcano toward H_2O_2 is the minimally intersecting region (convex hull) of the following selectivity free energy inequalities:

$$\Delta G_{O_{2(g)}+H^*\rightarrow OOH^*} < \Delta G_{O_{2(g)}+H^*+2*\rightarrow 2O^*+H^*} \quad (1)$$

$$\Delta G_{OOH^*+H^*+*\rightarrow H_2O_2^*+*} < \Delta G_{OOH^*+H^*+*\rightarrow O^*+OH^*+H^*} \quad (2)$$

$$\Delta G_{H_2O_2^*+*\rightarrow H_2O_{2(l)}+2*} < \Delta G_{H_2O_2^*+*\rightarrow 2OH^*} \quad (3)$$

$$\Delta G_{OOH^*+H^*\rightarrow H_2O_2^*+*} < \Delta G_{OOH^*+H^*\rightarrow H_2O_{(l)}+O^*+*} \quad (4)$$

These selectivity criteria can be thought of qualitatively in the following manner. Inequality constraint 1 represents the competition between O_2 dissociation and hydrogenation that is relevant early in the DHPSP. Constraint 2 represents the tendency of OOH* to hydrogenate to H_2O_2* as compared to its tendency to dissociate to OH* + O*. Constraint 3 represents the competition between desorption of H_2O_2* into the solution phase as $H_2O_{2(l)}$ and dissociation into 2OH* (which is rather facile on most metals). Finally, constraint 4 describes the competition of hydrogenating OOH* into either H_2O_2* or O* + $H_2O_{(l)}$. Since H_2 dissociation is an elementary step in all possible reaction pathways, we do not explicitly include this step in the selectivity criteria. As can be seen in Figure 5, the actual window in the Sabatier volcano where $H_2O_{2(l)}$ can be selectively formed is relatively small. It turns out that in our analysis only eqs 1, 3, and 4 are relevant in the descriptor range of interest; eq 1 is inclusive of eq 2 for all relevant values of ΔG_{O^*} and ΔG_{H^*}. The intersecting space of eqs 1, 3, and 4, where the governing chemistry and rate-limiting steps dictate the formation of peroxide by effectively preventing O_2, OOH*, and H_2O_2* dissociation, is found to the right, lower right, and upper right of the activity maximum; this region is delineated by thick black lines in Figure 5. All possible pathways involving water-mediated hydrogenation were also explicitly investigated. These additional selectivity constraints do not alter our conclusions, however, as they are only relevant outside of the peroxide space identified above. To reflect known uncertainties in DFT calculations and in the scaling and BEP correlations used, we have also added sensitivity error bars, based on ±10% deviations in the respective correlations' slopes; these are shown in Figure 5 as the diffuse gradient at the selectivity boundaries. We note that the selective mechanism in eq 4 switches from exergonic to endergonic at the boundary line; outside of the boundary line, both it and the competing unselective step are exergonic and cannot be differentiated in the context of our analysis (partial, but not completely selective, peroxide production might therefore still be observed immediately outside of this selectivity boundary). We further note that, because we treat the oxygen−oxygen bond cleavage in criterion 4 with a purely thermodynamic analysis that has no overbarrier, it gives a worst-case estimate for peroxide selectivity in this region of descriptor space.

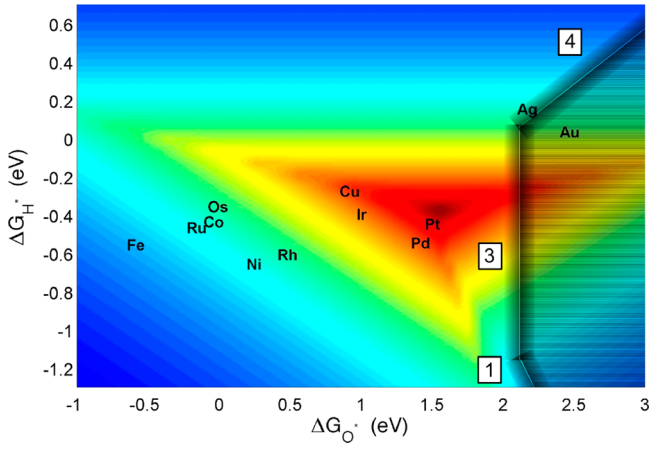

Figure 5. Selectivity boundaries for H_2O_2 formation on transition metal surfaces. The vertical line represents the competition between H_2O_2 desorption and dissociation, corresponding to selectivity eq 3 in the text. The other selectivity criteria, corresponding to eqs 1 and 4 in the text, represent the competition between O_2 hydrogenation and dissociation and between OOH hydrogenation and dissociation, respectively. The use of the black to gray gradient reflects estimated uncertainties in the location of the selectivity boundary. Other symbols have the same meaning as in Figures 3 and 4. The color scale of the underlying volcano is the same as in Figure 3.

Figure 5 strongly suggests that only pure metals as noble as Au meet all the free energy constraints defined above and will favor H_2O_2 production; Ag lies essentially on the error bars at the selectivity boundaries. This result, in turn, can be traced to the fact that less oxophilic metals, such as Au, are less likely to activate various forms of oxygen−oxygen bonds, thus favoring the direct hydrogen peroxide pathway in Figure 1. These results are additionally in very good agreement with recent experimental work. It is known, for example, that Au(111) is highly selective to hydrogen peroxide in electrochemical oxygen reduction,[59] while Ag can form mixed product phases of H_2O/H_2O_2.[59,60] Single-element transition metal catalysts near the Sabatier volcano maxima (e.g., Cu, Pd, and even Pt[61−64]), on the other hand, will either not form surface-adsorbed H_2O_2 intermediates in the first place or should see these intermediates rapidly dissociated into other surface intermediates that will, in turn, lead to surface oxidation or water formation. We note that, in industrial heterogeneous synthesis conditions, monometallic Pd has been used as an H_2O_2 production catalyst; in some cases, reasonable activities and ∼50% selectivities can be obtained in the best

dx.doi.org/10.1021/cs3003337 | ACS Catal. 2012, 2, 2664−2672

cases.[65−69] We further note, however, that these selectivities are highly influenced by promoter and support effects, which are not the focus of the present study. Additionally, we have considered the ability of Pd(111) to uptake subsurface hydrogen from $H_{2(g)}$ in high pressure and reducing environments, together with the impact of this subsurface H on hydrogen peroxide chemistry. We have performed a model calculation with a 1 ML octahedral H sublayer in our Pd(111) slab. The corresponding shifts in the surface H* and O* descriptor values are ∼0.15 and 0.45 eV, respectively, and are much closer to our predicted selectivity boundary. This result may explain why Pt(111) is not a viable H_2O_2 synthesis catalyst in heterogeneous conditions, as Pt does not uptake H to the extent Pd does.

3.4. Effects of Defects. The results presented above have focused on the defect-free flat surfaces of transition metals. Although such surfaces are generally the most prevalent features on realistic catalytic nanoparticles, it is also appropriate to consider the effect of model defects on the hydrogen peroxide reactivity trends described above. We have calculated the adsorption energies of the relevant adsorbates on the (211) surfaces of the fcc transition metals (Ag, Au, Pt, Pd), as well as approximate dissociation BEPs of the $2* + O_2 \rightarrow 2O*$ and $2* + H_2 \rightarrow 2H*$ reactions on these metals. The approximate shift of the volcano activity maximum due to the lowering of these two BEP barriers is ∼+0.2 eV on the O* axis and 0.1 eV on the H* axis; this observation is consistent with the general trend that Miller index terminated surfaces vicinal to fcc(111), such as fcc(211) facets, typically have lower activation barriers for many chemical reactions due to the presence of undercoordinated step edge atoms, and it has previously been seen in computed volcano plots for the electrochemical ORR.[22,70−73] More detailed selectivity analysis on the step surfaces would require additional calculations to determine the dissociation kinetics of oxygen−oxygen bond cleavage in both H_2O_2* and OOH* for many additional metals, but it is likely that the more active step edges would also promote more facile dissociation of these species, hence further shrinking the peroxide selectivity window compared to the defect-free surfaces. Recent work has shown that very small gold clusters have, in fact, evidenced significantly reduced kinetic barriers for O−O bond and related dissociation reactions.[74] A limited set of calculations for the H_2O_2 dissociation barrier (on Pd, Pt, Ag, and Au; this work) indicates that the oxygen−oxygen dissociation barrier is, in fact, lower on the steps than on the terraces (see Supporting Information), consistent with these intuitive analyses. Therefore, the most selective H_2O_2 synthesis catalysts are likely to be much larger nanoparticles with corresponding facets that offer large surface area fractions corresponding to the low index surfaces.

3.5. Prediction of New Catalysts. The results of our Sabatier selectivity volcano provide a natural optimization target for the computational identification of improved direct hydrogen peroxide synthesis catalysts. The optimal compromise between oxygen reduction activity and selectivity to hydrogen peroxide is approximately found in the ellipsoidal region of Figure 6. The location of this optimal region provides a simple and compelling explanation for the known suitability of AuPd alloys for direct hydrogen peroxide synthesis.[4,5,13] Parts of this region lie between pure Au and pure Pd on the Sabatier volcano, and according to the interpolation principle,[75,76] many AuPd alloys will likely fall in this region. This intuition is confirmed by explicit DFT calculations on Au−Pd near-surface alloys of different compositions. Some of the most promising of these points so far identified are shown in light purple in Figure 6. As is expected,

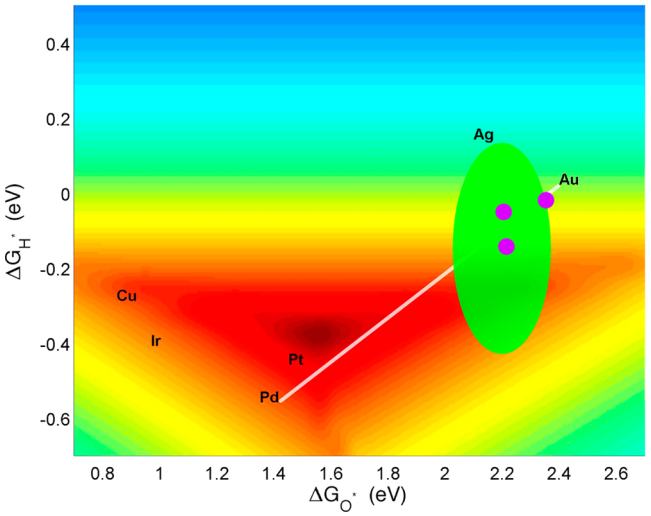

Figure 6. Results of initial alloy-based screening for catalysts that are active and selective for direct H_2O_2 synthesis. The white line represents a simple interpolation between Au and Pd. Purple dots represent alloys or skin overlayers of Pd−Au {clockwise from top, $Pd_4/Au_2Pd_2/Au_2Pd_2/Au_4$, $Pd_2Au_2/Pd_2Au_2/Pd_2Au_2/Pd_2Au_2$, $Pd_4/Au_2Pd_2/AuPd_3/Au_4$}. The green highlighted area represents the ideal target area for predicted optimally selective and active catalysts for direct hydrogen peroxide synthesis. The color scale of the underlying volcano is the same as in Figure 3.

the surface alloys indeed fall approximately in a range that balances the high activity of Pd and the high selectivity of Au, providing strong evidence for the explanatory power of our volcano and providing a basis for future computational screening efforts. We note that many of these promising candidate alloys lie near the intersection of the H_2 dissociation/OOH formation rate-limiting step regions of the computed volcano plot. Since previous work[77] on near-surface alloy/surface skin alloy catalysts involving Pt and Pd skins has shown significant reduction of overall H_2 dissociation barriers for given hydrogen binding energies relative to pure single-element constituent catalysts, it also may be possible to increase the overall catalyst activity in this region beyond what our volcano currently predicts. We further note that, while this screening analysis identifies possible alloys with appropriate descriptor-based properties, the stabilities of these alloys would need to be tested with further calculations and experiments. For example, while our volcano might suggest that Pt−Au alloys would also show promising properties for selective peroxide production, it is known that Pt−Au is more difficult to alloy in bulk and at the nanoscale than Pd−Au.[78,79] This is the likely reason why Pd−Au is the current state-of-the-art experimentally synthesized selective peroxide synthesis alloy nanocatalyst.[3−5]

4. CONCLUSIONS

We have performed comprehensive DFT calculations that characterize the reaction network involving the hydrogenation of O_2 by H_2 at the solid−liquid interface on the surface of 12 transition metals. We interpret these results with a simple Sabatier analysis and develop a volcano plot that expresses the catalytic activity as a function of two independent descriptors: the hydrogen and oxygen adsorption energies. Combining these results with a compact set of free energy inequalities that describe the selectivity to hydrogen peroxide production, we identify a region of descriptor space, generally corresponding to weak

dx.doi.org/10.1021/cs3003337 | ACS Catal. 2012, 2, 2664−2672

oxygen binding energies, that is an optimal compromise between activity and selectivity. Our results are in good agreement with known experimental trends and prior theoretical treatments of the electrochemical oxygen reduction reaction. The results provide a powerful and intuitive explanation of why Pd−Au catalysts function well for selective hydrogen peroxide production and suggest a natural optimization target for future computational catalyst screening efforts. We anticipate that the approach of combining activity and selectivity in a single volcano plot, utilized in this paper, can be generally extended to help understand other challenging reaction networks where product (or intermediate) metastability and selectivity are challenging issues to predict and characterize.

■ ASSOCIATED CONTENT

Supporting Information

Additional information about calculated lattice constants, details of free energy calculations, scaling relationships, transition state energy determinations, electronic convergence data, prefactor determination, and selected free energy pathways. This material is available free of charge via the Internet at http://pubs.acs.org.

■ AUTHOR INFORMATION

Corresponding Author

*E-mail: jgreeley@anl.gov.

Notes

The authors declare no competing financial interest.

■ ACKNOWLEDGMENTS

A DOE Early Career Award for J.G., as well as use of the Center for Nanoscale Materials, was supported by the U.S. Department of Energy, Office of Science, Office of Basic Energy Sciences, under Contract No. DE-AC02-06CH11357. The research was partially performed using EMSL, a national scientific user facility sponsored by the Department of Energy's Office of Biological and Environmental Research and located at Pacific Northwest National Laboratory. We gratefully acknowledge use of "Fusion", a computing cluster operated by the Mathematics and Computer Science Division at Argonne National Laboratory as part of its Laboratory Computing Resource Center. Helpful discussions with Maria K. Chan are appreciated.

■ REFERENCES

(1) Goor, G.; Glenneberg, J.; Jacobi, S. In *Ullmann's Encyclopedia of Industrial Chemistry*; Wiley: New York, 2007.
(2) Lunsford, J. H. *J. Catal.* **2003**, *216*, 455.
(3) Edwards, J. K.; Solsona, B.; Landon, P.; Carley, A. F.; Herzing, A.; Watanabe, M.; Kiely, C. J.; Hutchings, G. J. *J. Mater. Chem.* **2005**, *15*, 4595.
(4) Edwards, J. K.; Solsona, B.; N, E. N.; Carley, A. F.; Herzing, A. A.; Kiely, C. J.; Hutchings, G. J. *Science* **2009**, *323*, 1037.
(5) Edwards, J. K.; Carley, A. F.; Herzing, A. A.; Kiely, C. J.; Hutchings, G. J. *Faraday Discuss.* **2008**, *138*, 225.
(6) Edwards, J. K.; Solsona, B. E.; Landon, P.; Carley, A. F.; Herzing, A.; Kiely, C. J.; Hutchings, G. J. *J. Catal.* **2005**, *236*, 69.
(7) Choudhary, V. R.; Jana, P. *J. Catal.* **2007**, *246*, 434.
(8) Choudhary, V. R.; Samanta, C. *J. Catal.* **2006**, *238*, 28.
(9) Choudhary, V. R.; Samanta, C.; Jana, P. *Appl. Catal., A: Gen.* **2007**, *317*, 234.
(10) Li, G.; Edwards, J.; Carley, A. F.; Hutchings, G. J. *Catal. Today* **2007**, *122*, 361.
(11) Li, G.; Edwards, J.; Carley, A. F.; Hutchings, G. J. *Catal. Commun.* **2007**, *8*, 247.
(12) Ford, D. C.; Nilekar, A. U.; Xu, Y.; Mavrikakis, M. *Surf. Sci.* **2010**, *604*, 1565.
(13) Ham, H. C.; Hwang, G. S.; Han, J.; Nam, S. W.; Lim, T. H. *J. Phys. Chem. C* **2009**, *113*, 12943.
(14) Nakamura, M.; Sato, N.; Hoshi, N.; Sakata, O. *Langmuir* **2010**, *26*, 4590.
(15) Rossmeisl, J.; Karlberg, G. S.; Jaramillo, T.; Norskov, J. K. *Faraday Discuss.* **2009**, *140*, 337.
(16) Norskov, J. K.; Bligaard, T.; Rossmeisl, J.; Christensen, C. H. *Nat. Chem.* **2009**, *1*, 37.
(17) Greeley, J.; Rossmeisl, J.; Hellmann, A.; Norskov, J. K. *Z. Phys. Chem.* **2009**, *221*, 1209.
(18) Ferrin, P.; Nilekar, A. U.; Greeley, J.; Mavrikakis, M.; Rossmeisl, J. *Surf. Sci.* **2008**, *602*, 3424.
(19) Falsig, H.; Hvolbæk, B.; Kristensen, I. S.; Jiang, T.; Bligaard, T.; Christensen, C. H.; Nørskov, J. K. *Angew. Chem., Int. Ed.* **2008**, *47*, 4835.
(20) Stamenkovic, V.; Mun, B. S.; Mayrhofer, K. J. J.; Ross, P. N.; Markovic, N. M.; Rossmeisl, J.; Greeley, J.; Nørskov, J. K. *Angew. Chem., Int. Ed.* **2006**, *45*, 2897.
(21) Greeley, J.; Jaramillo, T. F.; Bonde, J.; Chorkendorff, I.; Norskov, J. K. *Nat. Mater.* **2006**, *5*, 909.
(22) Nørskov, J. K.; Bligaard, T.; Logadottir, A.; Bahn, S.; Hansen, L. B.; Bollinger, M.; Bengaard, H.; Hammer, B.; Sljivancanin, Z.; Mavrikakis, M.; Xu, Y.; Dahl, S.; Jacobsen, C. J. H. *J. Catal.* **2002**, *209*, 275.
(23) van der Vliet, D. F.; Wang, C.; Li, D.; Paulikas, A. P.; Greeley, J.; Rankin, R. B.; Strmcnik, D.; Tripkovic, D.; Markovic, N. M.; Stamenkovic, V. R. *Angew. Chem.* **2012**, *124*, 3193.
(24) Hansgen, D. A.; Vlachos, D. G.; Chen, J. G. *Nat. Chem.* **2010**, *2*, 484.
(25) Toulhoat, H.; Raybaud, P.; Kasztelan, S.; Kresse, G.; Hafner, J. *Catal. Today* **1999**, *50*, 629.
(26) Greeley, J.; Nørskov, J. K. *Surf. Sci.* **2007**, *601*, 1590.
(27) Greeley, J.; Nørskov, J. K.; Kibler, L. A.; El-Aziz, A. M.; Kolb, D. M. *ChemPhysChem* **2006**, *7*, 1032.
(28) Mehmood, F.; Rankin, R. B.; Greeley, J.; Curtiss, L. A. *Phys. Chem. Chem. Phys.* **2012**, *14*, 8644.
(29) Liu, B.; Greeley, J. *Top. Catal.* **2012**, *55*, 280.
(30) Grabow, L. C.; Studt, F.; Abild-Pedersen, F.; Petzold, V.; Kleis, J.; Bligaard, T.; Nørskov, J. K. *Angew. Chem., Int. Ed.* **2011**, *50*, 4601.
(31) Studt, F.; Abild-Pedersen, F.; Bligaard, T.; Sorensen, R. Z.; Christensen, C. H.; Norskov, J. K. *Science* **2008**, *320*, 1320.
(32) Kresse, G.; Hafner, J. *Phys. Rev. B* **1993**, *47*, 558.
(33) Kresse, G.; Hafner, J. *Phys. Rev. B* **1994**, *49*, 14251.
(34) Kresse, G.; Furthmüller, J. *Phys. Rev. B* **1996**, *54*, 11169.
(35) Kresse, G.; Furthmüller, J. *Comput. Mater. Sci.* **1996**, *6*, 15.
(36) Blöchl, P. E. *Phys. Rev. B* **1994**, *50*, 17953.
(37) Kresse, G.; Joubert, D. *Phys. Rev. B* **1999**, *59*, 1758.
(38) Perdew, J. P.; Chevary, J. A.; Vosko, S. H.; Jackson, K. A.; Pederson, M. R.; Singh, D. J.; Fiolhais, C. *Phys. Rev. B* **1992**, *46*, 6671.
(39) Perdew, J. P.; Chevary, J. A.; Vosko, S. H.; Jackson, K. A.; Pederson, M. R.; Singh, D. J.; Fiolhais, C. *Phys. Rev. B* **1993**, *48*, 4978.
(40) Methfessel, M.; Paxton, A. T. *Phys. Rev. B* **1989**, *40*, 3616.
(41) Nilekar, A. U.; Mavrikakis, M. *Surf. Sci.* **2008**, *602*, L89.
(42) Ojifinni, R. A.; Froemming, N. S.; Gong, J.; Pan, M.; Kim, T. S.; White, J. M.; Henkelman, G.; Mullins, C. B. *J. Am. Chem. Soc.* **2008**, *130*, 6801.
(43) Mavrikakis, M.; Stoltze, P.; Nørskov, J. K. *Catal. Lett.* **2000**, *64*, 101.
(44) Henkelman, G.; Jonsson, H. *J. Chem. Phys.* **2000**, *113*, 9978.
(45) Henkelman, G.; Uberuaga, B. P.; Jonsson, H. *J. Chem. Phys.* **2000**, *113*, 9901.
(46) Jónsson, H.; Mills, G.; Jacobsen, K. W. *Nudged Elastic Band Method for Finding Minimum Energy Paths of Transitions*; World Scientific: Singapore, 1998.
(47) Sheppard, D.; Terrell, R.; Henkelman, G. *J. Chem. Phys.* **2008**, *128*, 134106.
(48) Nørskov, J. K.; Rossmeisl, J.; Logadottir, A.; Lindqvist, L.; Kitchin, J. R.; Bligaard, T.; Jónsson, H. *J. Phys. Chem. B* **2004**, *108*, 17886.

(49) *CRC Handbook of Chemistry and Physics*, 92nd ed.; CRC Press: Boulder, CO, USA, 2011.
(50) Kandoi, S.; Gokhale, A. A.; Grabow, L. C.; Dumesic, J. A.; Mavrikakis, M. *Catal. Lett.* **2004**, *93*, 93.
(51) Zeinalipour-Yazdi, C. D.; Efstathiou, A. M. *J. Phys. Chem. C* **2008**, *112*, 19030.
(52) Michaelides, A.; Alavi, A.; King, D. A. *J. Am. Chem. Soc.* **2003**, *125*, 2746.
(53) Greeley, J.; Stephens, I. E. L.; Bondarenko, A. S.; Johansson, T. P.; Hansen, H. A.; Jaramillo, T. F.; Rossmeisl, J.; Chorkendorff, I.; Nørskov, J. K. *Nat. Chem.* **2009**, *1*, 552.
(54) Okamoto, Y.; Sugino, O. *J. Phys. Chem. C* **2010**, *114*, 4473.
(55) Bligaard, T.; Nørskov, J. K.; Dahl, S.; Matthiesen, J.; Christensen, C. H.; Sehested, J. *J. Catal.* **2004**, *224*, 206.
(56) Ferrin, P.; Simonetti, D.; Kandoi, S.; Kunkes, E.; Dumesic, J. A.; Nørskov, J. K.; Mavrikakis, M. *J. Am. Chem. Soc.* **2009**, *131*, 5809.
(57) Abild-Pedersen, F.; Greeley, J.; Studt, F.; Rossmeisl, J.; Munter, T. R.; Moses, P. G.; Skúlason, E.; Bligaard, T.; Nørskov, J. K. *Phys. Rev. Lett.* **2007**, *99*, 016105.
(58) Norskov, J. K.; Bligaard, T.; Hvolbaek, B.; Abild-Pedersen, F.; Chorkendorff, I.; Christensen, C. H. *Chem. Soc. Rev.* **2008**, *37*, 2163.
(59) Blizanac, B. B.; Stamenkovic, V.; Markovic, N. M. *Z. Phys. Chem.* **2007**, *221*, 1379.
(60) Blizanac, B. B.; Ross, P. N.; Marković, N. M. *J. Phys. Chem. B* **2006**, *110*, 4735.
(61) Gasteiger, H. A.; Ross, P. N. *J. Phys. Chem.* **1996**, *100*, 6715.
(62) Stamenkovic, V.; Markovic, N. M.; Ross, P. N., Jr. *J. Electroanal. Chem.* **2001**, *500*, 44.
(63) Marković, N. M.; Gasteiger, H. A.; Grgur, B. N.; Ross, P. N. *J. Electroanal. Chem.* **1999**, *467*, 157.
(64) Todorovic, R.; Meyer, R. J. *Catal. Today* **2011**, *160*, 242.
(65) Chanchal, S. *Appl. Catal., A: Gen.* **2008**, *350*, 133.
(66) Ghedini, E.; Menegazzo, F.; Signoretto, M.; Manzoli, M.; Pinna, F.; Strukul, G. *J. Catal.* **2010**, *273*, 266.
(67) Melada, S.; Rioda, R.; Menegazzo, F.; Pinna, F.; Strukul, G. *J. Catal.* **2006**, *239*, 422.
(68) Ntainjua, E. N.; Piccinini, M.; Pritchard, J. C.; Edwards, J. K.; Carley, A. F.; Kiely, C. J.; Hutchings, G. J. *Catal. Today* **2011**, *178*, 47.
(69) Choudhary, V. R.; Samanta, C.; Choudhary, T. V. *Appl. Catal., A: Gen.* **2006**, *308*, 128.
(70) Xu, Y.; Mavrikakis, M. *Surf. Sci.* **2003**, *538*, 219.
(71) Xu, Y.; Mavrikakis, M. *J. Phys. Chem. B* **2003**, *107*, 9298.
(72) Rempel, J.; Greeley, J.; Hansen, L. B.; Nielsen, O. H.; Nørskov, J. K.; Mavrikakis, M. *J. Phys. Chem. C* **2009**, *113*, 20623.
(73) Greeley, J.; Rossmeisl, J.; Hellmann, A.; Norskov, J. K. *Z. Phys. Chem.* **2007**, *221*, 1209.
(74) Grabow, L.; Hvolbæk, B.; Falsig, H.; Nørskov, J. *Top. Catal.* **2012**, *55*, 336.
(75) Greeley, J.; Nørskov, J. K. *Surf. Sci.* **2005**, *592*, 104.
(76) Bligaard, T.; Honkala, K.; Logadottir, A.; Nørskov, J. K.; Dahl, S.; Jacobsen, C. J. H. *J. Phys. Chem. B* **2003**, *107*, 9325.
(77) Greeley, J.; Mavrikakis, M. *Nat. Mater.* **2004**, *3*, 810.
(78) Zhang, W.; Li, L.; Du, Y.; Wang, X.; Yang, P. *Catal. Lett.* **2009**, *127*, 429.
(79) Schrinner, M.; Proch, S.; Mei, Y.; Kempe, R.; Miyajima, N.; Ballauff, M. *Adv. Mater.* **2008**, *20*, 1928.